Highly ordered Pd, Fe, and Co clusters on alumina on Ni3Al(111)

Andreas Buchsbaum, Maurizio de Santis, Hélio Tolentino, Michael Schmid, Peter Varga

Highly ordered growth of Fe and Co clusters on alumina on $Ni_3Al(111)$

Andreas Buchsbaum[1], Maurizio De Santis[2], Helio C.N. Tolentino[2], Michael Schmid[1], Peter Varga[1]

1 Institut für Allgemeine Physik, Technische Universität Wien, A-1040 Wien, Austria

2 Institut Neel, CNRS & UJF, BP 166, 38042 Grenoble cedex 9, France

Template mediated growth of metals has attracted much interest due to the remarkable magnetic but also catalytic properties of clusters in the nanometer range and provides the opportunity to grow clusters with narrow size distributions. We have grown well-ordered Fe and Co clusters on the ultrathin aluminium oxide on $Ni_3Al(111)$, a template with a 4.1 nm lattice. The structure of the ≈ 0.5 nm thick oxide film exhibits holes reaching down to the metal substrate at the corners of the $(\sqrt{67} \times \sqrt{67})R12.2°$ unit cell. Pd atoms trapped in these corner holes create metallic nucleation sites where Fe as well as Co clusters can nucleate and form a well-ordered hexagonal arrangement on the oxide nanomesh.

We have studied the morphology of these Fe and Co clusters and applied different methods like scanning tunneling microscopy (STM) and surface x-ray diffraction (XRD) to determine the morphology and crystallographic of the clusters. For Fe we found cluster growth in either bcc[110] or bcc[100] direction, depending on the deposition temperature and for Co we found close-packed planes on top of the clusters and random stacking of fcc and hcp planes.

PACS: 61.46.Df, 68.47.Gh, 81.16.Dn, 63.22.Kn, 68.47.Jn, 78.67.Bf

I. Introduction

Template mediated growth of metals has attracted much interest not only due to the remarkable magnetic properties [1-18] but also due to catalytic properties [19-28] of clusters in the nanometer range. Intrinsic properties of bulk materials change as soon as surface and interface effects start to play a role. [1,3,4,7,10,11] Templates are not only a means to grow regularly arranged clusters but also provide the opportunity to grow clusters with a narrow size distribution by simple evaporation, taking advantage of the fact that the capture zones of equidistant clusters have equal area. Other techniques like colloidal chemistry, soft landing from the gas phase or deposition of clusters from the liquid phase give less control over either the arrangement or the size distribution of the clusters. Thus, self assembly on template surfaces is a perfect way of growing well-defined arrays of nanoclusters. [3,14,15,17,29-34]

Nanoparticles (e.g. colloidal Co nanoparticles [35,36]) used in catalysis offer not only the advantage of a large surface area available for the catalytic reaction but also the presence of catalytically active sites on different facets and on the edges of the nanoparticle. [27,28] Recent studies of oxide supported metal nanoparticles show an enhanced catalytic activity of nanoparticles in the presence of oxide phases. [37-42] Growing nanoparticles with well-defined size and structural properties is an essential prerequisite to understand the details of adsorbate-surface interactions and finally the catalytic reaction.

An essential characteristic for technological applications of nanostructures made of magnetic materials such as Fe and Co (e.g. magnetic storage media) is the magnetocrystalline anisotropy energy (MAE), which affects the thermal stability of the collective magnetic moments of nanostructures in the superparamagnetic state. [3,4,5,6,11,13,14,15,17,18] Besides the dependence of the MAE on the material, the size and

shape of the clusters are crucial. Many previous investigations show an enhanced MAE and orbital magnetic moment for structures in the subnanometer and nanometer range compared to the respective bulk systems due to the lower symmetry of atoms at the surface. [3,4,7,9,10,16] For proper investigations and applications of magnetism at the nanoscale, obtaining clusters with well-aligned easy axes and monodisperse size distribution is a key challenge in order to obtain well-defined magnetic properties. [3,4,5,6,7,13,17] Therefore, a detailed investigation of the morphology and the crystallography is required to understand magnetic and catalytic properties of nanostructures.

In particular, ultra-thin alumina on $Ni_3Al(111)$ offers ideal properties for template mediated growth of self-organized 2-dimensional arrays of clusters. This template is especially useful because it combines large distances between the nucleation sites (4.1 nm) with the possibility to grow three-dimensional clusters, allowing us to tune the cluster size in a range of more than two orders of magnitude. The structure of this ≈ 0.5 nm thick oxide film, which has been solved recently,[43] exhibits holes reaching down to the metal substrate. These holes, located at the corners of the ($\sqrt{67} \times \sqrt{67}$)R12.2° unit cell, are large enough to trap any kind of metal atoms, but only Pd atoms have been trapped in these holes so far. The applicability of this alumina film as a template with a 4.1 nm lattice for growing well-ordered metal clusters of Pd and Pd/Au has been noted already before the structure of the oxide was known. [44,45] The unmodified oxide is not a good template for most other metals, [46,47,48] which was explained by a barrier for other metal atoms preventing them from jumping into these corner holes.[43] We have shown that the corner holes can be filled with Pd atoms and, hence, a metallic nucleation site can be created where other metal atoms such as Fe and Co can nucleate and form a well-ordered arrangement, too.[43] In the current work,

we exploit this method and study the morphology and structure of these clusters in detail.

II. Experimental Setup

Scanning tunneling microscopy (STM) measurements were carried out in Vienna, in an ultrahigh vacuum (UHV) system with a base pressure below 10^{-10} mbar. For cleaning the surface of the $Ni_3Al(111)$ crystal, we used 2 keV Ar^+ sputtering and annealing to roughly 1100 K. The cleanliness of the crystal surface was verified by Auger electron spectroscopy (AES) and STM. As high temperatures would lead to evaporation of Al from the surface, the annealing temperature should not significantly exceed 1100 K. The alumina film was grown at a temperature of 1000 K and an oxygen pressure of $3 \times 10^{-9} - 5 \times 10^{-9}$ mbar for several hours; this typically corresponds to a dose of ≈ 40 Langmuir (1 Langmuir = 10^{-6} torr·s). Compared to higher pressures but the same oxygen dose, slower oxidation results in a more homogenous surface, covered with the (√67 × √67)R12.2° phase over large areas and fewer domain boundaries. By this preparation procedure the formation of the other phases, i.e., the "stripe" phase [49] and the hexagonal (√79 × √79)R17° oxide phase also observed on this surface,[43] could be avoided. The exact preparation procedure for growth of the desired (√67 × √67)R12.2° oxide structure is not exactly the same for all single crystals of nominal composition Ni_3Al; e.g. some crystals may require post-annealing at approx. 1150 K after oxidation; we consider it likely that the exact stoichiometry of the crystal plays a role.[43]

Deposition of palladium, cobalt and iron was done using liquid-nitrogen cooled electron beam evaporators (Focus EFM3). High-energy ions have been deflected by a

retarding-voltage applied at the end of the nozzle of the evaporator to avoid creation of defects in the oxide film which could act as additional nucleation centers for metal atoms [50]. The deposition rate was calibrated by a quartz crystal microbalance.

The STM measurements have been obtained at room temperature (RT) in constant current mode using a customized commercial STM (Omicron μ-STM) and an electrochemically etched W tip. All preparations made in this system have been checked by STM after oxidation and deposition of 3 Pd atoms per unit cell respectively, previous to the deposition of Fe or Co clusters, in order to verify a good quality of the template surface.

In addition to STM, structural properties of Co and Pd clusters were investigated by surface x-ray diffraction (SXRD) in the *Surface under Ultra-high Vacuum* (SUV) laboratory of the beamline BM32 at the European Synchrotron Radiation Facility (ESRF) in Grenoble. The experimental setup allows the simultaneous in-situ measurement of grazing incidence small angle x-ray scattering (GISAXS) during deposition of the clusters with water-cooled electron beam evaporators (Focus EFM4) from the onset of cluster formation to coalescence. SXRD and GISAXS measurements were done at a wavelength of $\lambda = 0.06262$ nm. The incident angle α_i of the x-ray beam for SXRD was 0.5° and for GISXAS measurements 0.2° (Fig. 6), very close to the critical angle for total reflection [51]. For these measurements, we have used a crystal well characterized by STM; in addition, prior to the x-ray measurements the sample preparation was checked with reflection high-energy electron diffraction and AES.

III. Results and Discussion

A. The oxide

The aluminum oxide used in this work as a template for growing well-ordered metal clusters has a (√67 x √67)R12.2° unit cell (related to the $Ni_3Al(111)$ surface) with a p6 symmetry.[52] Fig. 1 shows two STM images of the alumina film measured at a tunneling voltage of 3.1 V (a), where the "network structure" appears, and 2.3 V (b), respectively, to visualize the "dot structure".[52,53] In both images two unit cells are drawn at the same position of the sample. The corners of the unit cells are sixfold symmetry axes of the oxide film and marked by hexagons; the two threefold axes in the cell are marked by triangles in Fig. 1(b). The sixfold sites at the corner of the unit cell are visible as dark depressions in the "network structure" or bright protrusions in the "dot structure"; these are holes down to the metallic substrate as described above; see Ref. [43] for more details. Also the threefold sites are defects; there an Al triangle is found at the metal-oxide interface instead of the usual Al hexagons, with three instead of 2 interface Al atoms binding to oxygen. Besides the sixfold and threefold sites the oxide exhibits defects, which are visible in Fig. 1(b) as small bright dots (some marked by circles), less prominent than the corner holes. These extra defects possess no strict long-range order, but they are all close to a threefold axis of the unit cell.

While STM images taken at 2.3 V are advantageous to reveal the ordering of the oxide and the extra defects (Fig. 1b), we employ STM images taken at 3.1 V to study the geometrical properties of metal clusters grown on top of the oxide (see below).

B. Fe and Co nucleation on the unmodified oxide

In general, metals on oxide surfaces have a low work of adhesion and clusters growing on oxide films show bad wetting [54] while thin metal films on metal surfaces

show good wetting and layer-by-layer growth in many cases. [55] Particularly it has been shown for the very similar alumina film on NiAl(110) that Pd and Co clusters exclusively nucleate on defects and on step edges. [56] Moreover the high chemical affinity between Al and O atoms should not allow Fe and Co atoms to bond to any oxygen atom of a defect-free oxygen-terminated alumina surface. Thus, the lowest energy for metal atoms deposited on alumina on $Ni_3Al(111)$ would be in the corner holes, followed by defects.

Fig. 2 shows two STM images taken at 3.1 V where (a) 0.1 nm Fe and (b) 0.06 nm Co has been deposited at RT on the clean oxide surface. The coverages stated in this work are readings of a quartz-crystal microbalance, i.e., the film thickness averageed over the sample area, assuming bulk density. At first glance the arrangement of the Fe clusters in Fig. 1a seems to be random without any long-range order. However, the upper insert in Fig. 2a shows a fast Fourier transform (FFT) of a map derived from the STM image where only the cluster centers are marked as points. The sharp spots in the FFT correspond to a distance of $4.1/\sqrt{3}$ nm, i.e., the periodicity of the "network structure". The lower inset shows an STM image taken at 2.3 V of 0.01 nm Fe deposited at the same conditions with the same scale as the large STM image of Fig. 2a. As mentioned before, at this voltage the corner holes appear bright and are marked as cross points of the white lattice. The arrows in the inset mark the Fe clusters. In this image it is clearly visible that the nucleation sites of Fe atoms neither match the corner holes nor other high-symmetry positions of the lattice. We consider it likely that Fe clusters nucleate at the extra defects described above [circles in Fig. 1(b)]. Thus, clusters nucleating on these defects occupy positions close to the threefold sites, but only a subset of the threefold sites have a cluster nearby. Nevertheless, sharp spots appear in the FFT of the cluster positions. Both the partial occupation and random

deviations from the threefold site only increase the background, but do not lead to blurring of the spots (this is comparable to the Debye-Waller factor in diffraction). Therefore it can be concluded that these defects are the main nucleation sites for Fe atoms on the unmodified oxide.

Fig. 2b shows the Co clusters deposited at RT. Similar to Fe, Co atoms do not nucleate in the corner holes, which are marked as the cross points of the white lattice in Fig. 2b. Obviously, Co nucleates close to or at the three fold axes of the unit cell, thus it forms a honeycomb lattice, with the corner holes left empty. As Co occupies a larger fraction of the threefold sites, the long-range order of its lattice is more apparent than that of Fe. This indicates that Co occupies also regular threefold sites that do not have a defect nearby. As mentioned above, neither Fe nor Co can overcome the barrier to jump into the corner hole at RT.[43] Increasing the temperature does not help; our STM experiments have shown that at temperatures above 570 K metal atoms nucleated in the corner hole become invisible, which we attribute to diffusion of metal atoms from the bottom of the corner hole into the Ni_3Al bulk or below the aluminum oxide. Hence, the deposition temperature is limited to 570 K.

C. Fe and Co nucleation with predeposition of Pd

As mentioned above, in contrast to Fe and Co atoms, Pd atoms are trapped in the corner holes, indicating a small or vanishing barrier for Pd. In Ref. [43] it is demonstrated that the hole is large enough to be filled with three Pd atoms without creating an adatom. This result suggests to create a template with well-ordered metallic dots embedded in the oxide, i.e., the Pd atoms in the corner holes, by predeposition of 3 Pd atoms per corner hole (3 Pd atoms per unit cell; this corresponds to an average coverage of 0.003 nm). From now on we will refer to predeposition of 3 Pd atoms as Pd seeded. If we think of the barrier for Fe or Co

atoms as some kind of Ehrlich-Schwoebel barrier step edges [57,58] [Fig. 3(a)], then we can obviously reduce the barrier by filling the holes and thereby allow Fe and Co atoms to nucleate on top of the Pd atoms in the corner holes.

Fig. 4 shows two STM images of (a) 0.1 nm Fe clusters and (b) 0.06 nm Co clusters (Pd seeded). Pd, Fe and Co have been deposited at RT. In both cases, Fe as well as Co, all Pd-filled corner holes are covered by a cluster (cross points of the white lattice). Fig. 4(a) shows that Fe clusters now nucleate almost exclusively on top of the corner holes. However, Co clusters now occupy both nucleation sites, the corner holes and the 3-fold sites of the unit cell [Fig. 4(b)]. Hence, the density of Co clusters is roughly 3 times the density of the Fe clusters.

The inset in Fig. 4 shows an STM image of the alumina with holes each filled by 3 Pd atoms in average and taken at 3.1 V (prior to Fe or Co cluster deposition). In contrast to empty corner holes of the unmodified oxide [dark corner hole, see Fig. 1(a)], filled corner holes appear flat or as protrusions in the STM image (gray or bright). We note that not all corner holes appear equally bright which is easily explicable as the number of Pd atoms will not be exactly 3 in all corner holes. Nevertheless, it seems that the distribution of the number of Pd atoms per corner hole is narrower than a purely statistical (Poisson) distribution. In that case, we would expect 20% of all corner holes to be filled with less than 2 Pd atoms. Given the atomic diameter of Pd (0.275 nm) and the thickness of the oxide (≈0.5 nm), we consider it very unlikely that a single Pd atom lying deep at the bottom of a corner hole would be sufficient for Co or Fe to overcome the step barrier. After Co or Fe deposition we find, however, that almost 100% of the corner holes are occupied by clusters (from a statistical distribution 80% would be expected). This indicates that the distribution of the number of Pd atoms per corner hole is narrower than a statistical distribution, probably because excess Pd

outside the hole (i.e., the 4th Pd atom) is bound more weakly than the Pd in the hole and diffuses to a site with stronger binding. We believe that almost all holes are filled with at least 2 Pd atoms and cluster vacancies (dark spots in the STM images) only appear at defects of the oxide where the corner hole is missing.

As mentioned above, the oxide with holes filled with Pd atoms can be heated to ≈ 570 K after Pd deposition without a modification of the template surface due to diffusion of Pd atoms from the bottom of the corner hole into the Ni_3Al bulk or below the aluminum oxide. One can therefore use this template for deposition of Fe and Co clusters at elevated temperatures up to 570 K. Fig. 5 shows 0.1 nm Fe (a) and 0.06 nm Co (b) clusters deposited at 470 K after filling the corner holes with 3 Pd atoms. Fe clusters deposited at 470 K show good ordering, i.e., they nucleate at the Pd-filled corner holes. This is not very different from the situation found of the RT deposition, apart from fewer clusters nucleated at defects between the corner holes (Fig. 5a). Co clusters, nucleating also on top of the 3-fold sites when deposited at RT, now grow on top of the corner holes only, similar to Fe (Fig. 5b). Hence, the additional kinetic energy of the Co atoms at 470 K is sufficient for escape from the potential energy well at the 3-fold sites, and Co nucleation in these sites is suppressed.

By combining the results from above we can schematically draw the potential energy surface for Fe and Co adatoms on the clean oxide and the modified oxide with corner holes filled by Pd atoms (Fig. 3b). The corner hole is the deepest well in the energy potential surface, i.e., the most favorable adsorption site (hexagons in Fig. 3b), but only accessible for Fe or Co when filled with Pd atoms (bottom panel; filled hexagons). Without predeposition of Pd, an energy barrier prevents Fe and Co from jumping into the empty corner hole. By filling the corner holes with Pd the barrier

vanishes for Fe and Co. The second best nucleation sites are the defects and the threefold sites (open circles and triangles in Fig. 3b). Nucleation at these sites is different for both metals; obviously the energy minimum at the threefold sites of the ideal oxide structure is to shallow for nucleation of Fe atoms but for Co it is deep enough to allow nucleation at these sites. They are no stable nucleation sites for single Fe atoms on the defect-free unmodified oxide. Also the defects close to the threefold sites are not very favorable for formation of stable Fe nuclei, i.e, rather shallow minima of the potential energy for Fe adatoms as indicated in Fig. 3(b). As soon as deep sinks for Fe atoms are created by pre-deposition of Pd it will be improbable for Fe atoms to meet at the defects on the oxide, which would be required to form a stable nucleus. Therefore, after predeposition of Pd, only few clusters can be found between the corner holes (Fig. 5a). For Co atoms the threefold sites are stable nucleation sites up to a deposition temperature of about 470 K. We cannot determine the significance of the extra defects for Co. These defects are close to the threefold sites of the unit cell, thus we cannot distinguish between Co clusters at a threefold site and one at a defect. Given the similarity of most properties of Fe and Co, we consider it likely that Co clusters nucleate on these defects instead of the perfect threefold site if a defect is available. Possibly there is also one broad energy minimum extending between the defect and the threefold site next to it.

The difference in RT growth between Fe and Co may be related to a deeper potential well for Co at the threefold sites as suggested in Fig. 3(b) and/or it may be the consequence of a different size of the critical nucleus: In the gas phase, bonding in the Co_2 molecule is much stronger (167 kJ/mol) than in Fe_2 (75 kJ/mol); the values on the oxide are probably somewhat lower. This suggests that an Fe_2 dimer on the oxide is

not stable at RT while Co_2 should be stable, and hence, creation of a stable nucleus should be more easy for Co than for Fe.

D. GISAXS of well ordered Co clusters

Prior to SXRD (see below), GISAXS measurements were done at the ESRF in Grenoble in order to verify the spatial arrangement of the clusters and, thus, a proper preparation of the aluminum oxide film. Fig. 6a shows a schematic view of the geometry used for the GISAXS measurements. The GISAXS measurements were done in-situ during deposition of Co clusters at 470 K (Pd seeded) on top of the oxide.

Fig. 6b–d show the images obtained at three different Co coverages; the inserts show corresponding STM images acquired in separate experiments with the same growth conditions and the same coverage. Fig. 6b has been taken after the onset of cluster formation at a coverage of 0.18 nm. The direction of the incident x-ray beam has been aligned in the (11) direction of one superstructure domain, i.e., parallel to a close-packed row of clusters. Therefore, the in-plane coordinate $q_{||}$ of the GISAXS contains the information about the spatial arrangement of the clusters. The two side maxima correspond to the distance of the rows of clusters, which is $4.1 \times \sqrt{3}/2$ nm in real space (sketch in Fig. 6a). Hence, these correlation peaks, found at $q_{||} = \pm 1.77$ nm^{-1} in reciprocal space, confirm the arrangement visible in the STM images. Already at a Co coverage of 0.18 nm we find a weak background at lower $q_{||}$ (Fig. 6a) corresponding to larger distances in real space. This background becomes stronger with increasing coverage. Below coalescence of the well-ordered clusters, this distribution is attributed to areas with badly ordered clusters at domain boundaries or areas with a disordered oxide. The GISXAS measurement shown in Fig. 6c was taken at a Co

coverage of 0.54 nm, soon after the onset of coalescence of clusters when the correlation peaks start to diminish. The corresponding STM image shows coalescence of some of the clusters. Due to coarsening, new broad peaks appear at $q_{||} = \pm 0.96$ nm^{-1}. With increasing coverage, these peaks move towards lower $q_{||}$ and broaden due to a loss of correlation. According to STM and GISAXS data coalescence is completed at a coverage of 1 nm, shown in Fig. 6c. At this stage, GISAXS as well as Fourier-transformed STM images show a complete loss of the original hexagonal arrangement of the clusters, and the peak in the reciprocal space is at $q_{||} = \pm 0.71$ nm^{-1}, which corresponds to a typical distance of clusters in real space of 8.8 nm. This is in good agreement with the result of the STM images taken at the limit of coalescence where the calculated Radial Autocorrelation Function shows a typical distance between the clusters of 9.3 nm.

Line profiles parallel to the $q_{||}$ direction of the correlation peaks in the 2D GISAXS measurements are an indicator of the correlation length and, hence, the domain size. Before coalescence we find a width at half maximum (FWHM) of the peaks of roughly 0.1 nm^{-1}. This corresponds to 60 nm in real space, which is in good agreement with the domain size found by STM.

E. Height distributions of well ordered Fe and Co clusters

As a first step to determine the morphology of the clusters, we need to measure their height. At low coverages, where the oxide surface between the clusters can be still reached by the STM tip, we can measure the cluster height by STM. Unfortunately, this is not straightforward. If thin layers of insulators are measured by STM the

apparent height of the insulating layer is significantly different from the geometric height [59] and depends on the tunneling voltage [56,60,61]. In particular, for a bias voltage that lies in the band gap of the oxide, the oxide appears thinner than the real thickness, i.e., the tunneling current is low due to a lack of states available for tunneling. We follow the procedure in Ref. [56], where bias-voltage dependant height measurements have been made in order to determine the geometric heights of the clusters.

Fig. 7a shows the average height of well-ordered Fe clusters as a function of the tunneling voltage. The clusters were obtained by RT deposition of 0.06 nm Fe, i.e., in average 107 Fe atoms per cluster (Pd seeded). The oxide, measured at tunneling voltages in the band gap, will always appear thinner than it's geometrical thickness (0.5 nm), therefore the clusters will appear too high in this voltage range. In other words, the maximum apparent height measured for voltages in the bandgap is an upper limit of the cluster height. On the other hand the apparent height of the oxide must be larger than zero and, hence, from Fig. 7a we conclude that the real cluster height is in the range of 0.3 to 0.7 nm. At to the conduction band edge, between 2 and 3 V, the apparent height of the oxide increases and thus the apparent height of the clusters clusters drops decreases. Therefore, we expect an apparent height of the clusters that is close to the real one at voltages near the conduction band edge. In this work the STM images were usually acquired at 3.1 V.

Fig. 7(b) shows a height histogram of Fe cluster heights measured at 3.1 V (based on the same preparation as Fig. 7a). Two distinct peaks are visible; the peak separation is 0.14 nm, which can be identified as the interlayer distance of Fe bcc (100) planes (0.143 nm). According to the arguments presented above, the apparent height at this voltage must be close to the true cluster height [cf. Fig. 7(a)]. As the peaks must correspond to an integer multiple of the interlayer distance, i.e., 0.14 nm, they could

correspond to either 3 and 4 ML or 4 and 5 ML [the top axis of Fig. 7(b, c) assumes that the apparent height of the oxide at 3.1 V is equal to its true height]. If we assume truncated spheres to be the clusters shape, for a given height and number of Fe atoms per cluster (107 atoms per cluster) the diameter of the cluster can be easily calculated [56]. Assuming that the Fe cluster heights of the peaks in Fig. 7(b) correspond to 3 and 4 ML, this calculation would result in an average cluster diameter of 2.6 nm, which is in contradiction to the diameter visible in STM (< 2.4 nm). For cluster heights of 4 and 5 ML the calculation results in an average diameter of 2.2 nm, a size that seems to be realistic according to the STM images. Hence, for obtaining the true (geometrical) height of clusters, roughly 0.09 nm has to be added to the apparent height at 3.1 V.

We have also determined the cluster heights of Fe clusters deposited at 570 K (Pd seeded) [Fig. 7(c)]. In this case, the mean coverage was 0.1 nm, resulting in an average cluster size of 160 Fe atoms per cluster. In contrast to growth at RT, now the distance of the peaks in the clusters heights histogram is not 0.14 nm but 0.2 nm, which is close to the interlayer distance of Fe bcc(110) planes (0.202 nm). This means that the crystallographic orientation of the Fe clusters depends on the deposition temperature.

For Co clusters, Fig. 8 shows the voltage dependant height (a) and a height histogram (b) of well-ordered Co clusters obtained by deposition of 0.06 nm at 470 K (Pd seeded). This corresponds to an average size of 80 Co atoms per cluster. The average height of the Co clusters measured as a function of the tunneling voltage shows a similar behavior as Fig. 7(a), dominated by the oxide, not the metal. According to Fig. 8(a) the height of the Co clusters is limited to the range of 0.4 up to 0.7 nm. In the height histogram, again measured at 3.1 V tunneling voltage, the peaks are separated by 0.2 nm, which is the interlayer distance of close-packed Co planes, i.e., either

fcc(111) or hcp(0001) planes. For 0.1 nm well-ordered Co clusters (145 Co atoms per cluster) deposited at 570 K (Pd seeded) the same interlayer distance is found [Fig. 8(c)].

In Fig. 8(b), we can assign the main peak to either 2 or 3 ML. Repeating the calculation described above we can exclude 2 ML because the cluster diameter would be calculated to be 2.6 nm, incompatible with the STM images (< 2.3 nm). If we assume a thickness of 3 ML for the majority of the clusters [i.e., the main peak in Fig. 8(b)] the result of the calculation is an average cluster diameter of 1.8 nm, so we conclude that this value is the correct one. The correction of the cluster height therefore amounts to 0.07 nm, similar to the one for the Fe clusters shown above.

For metal clusters we can assume that the difference between true and apparent height does not strongly depend on the cluster material. Hence, the correction for converting the apparent height measured at 3.1 V bias into a geometric height should be roughly the same for all Fe and Co clusters; the exact value can be determined by the requirement that an integer number of layers should be found. Here we have neglected a problem caused by the finite resolution of the STM, however: The clusters appear smeared out in the STM images, i.e., they appear lower. So we expect that we to have to add a slightly higher correction for small clusters, which have a smaller radius of curvature (smaller top facet), leading to underestimation of the cluster height; conversely, for larger clusters the correction should be slightly lower. This may explain the fact that the apparent cluster heights of the larger clusters [Figs. 7(c), 8(c)] are somewhat closer to an integer number of monolayers than those for the smaller ones [Figs. 7(b), 8(b)].

F. Contact angle of well ordered Fe and Co clusters

As the distance and the spatial arrangement of the clusters is known the drift in the STM images can be easily corrected and the density of the clusters can be measured from the STM images. From the known volume of the clusters, i.e., the average number of atoms per cluster and their height, we can calculate the diameters and the contact angles by the equations given in Ref. [56]. The results for Fe and Co clusters deposited at different coverages and deposition temperatures, all Pd seeded, are given in Tab. 1. We note that contact angle increases with increasing deposition temperature. This can be easily explained by a higher mobility of Fe and Co atoms at the surface at elevated temperatures, which allows more atoms to jump onto the top terraces of the clusters and thereby the clusters grow higher than at low temperatures. At constant temperatures, we find that the contact angle does not depend significantly on the cluster size.

We consider it likely that the contact angle obtained at 570 K corresponds to thermodynamic equilibrium; this value is about 80° for both types of clusters, lower than the contact angle of ≈120° found for Co clusters found on NiAl(110).[56] This indicates a higher adhesion energy of the clusters on the oxide on $Ni_3Al(111)$, which might be due to the lower stability (higher surface energy) of this oxide compared to that on NiAl(110).

G. Structure of Fe and Co clusters after coalescence

For small clusters below coalescence, STM with atomic resolution on top of single clusters is not possible due to the high surface curvature. However, for high coverages

above coalescence, some of the clusters show flat facets on top where atomic resolution is possible. Fig. 9 shows strongly high-pass filtered STM images of 2.8 nm Fe (a) and Co (b) clusters above coalescence deposited at 470 K (Pd seeded).

In these STM images two different cluster species are visible: small distorted clusters with a wrinkled top and a few larger flat clusters. The fraction of flat clusters depends on the temperature of deposition. Below 470 K deposition temperature, small wrinkled Fe or Co clusters are the dominant species while at higher deposition temperatures larger flat clusters can be seen more frequently. A possible explanation for the wrinkled clusters is lattice mismatch of neighboring clusters, e.g. due to different azimuthal orientation of the lattices, leading to polycrystalline clusters upon coalescence. The insets of Fig. 9 are atomically resolved STM images 3 nm wide taken on top of one of the flat clusters visible in the STM images. Both show a surface with roughly 6-fold symmetry, i.e., bcc(110) for Fe clusters and close-packed plane for Co. Hence, the STM images with atomic resolution of clusters above coalescence agree well with the cluster orientation derived from height histograms of clusters below coalescence.

H. SXRD of Pd and Co clusters after coalescence

Unfortunately, STM does not allow us to distinguish between fcc and hcp close-packed Co planes. Hence, SXRD measurements were carried out to clarify this remaining question, which is essential for understanding the magnetic properties [62,63,64,65]. In the following, we index the reflections using the hexagonal cell of $Ni_3Al(111)$ surface, with the in plane lattice constant a = 0.5022 nm (the $Ni_3Al(111)$ cell being twice as large as its fcc lattice) and the out of plane one c = 0.6151 (3 layers according to the fcc stacking of Ni_3Al). Fig 10(a) shows a map of the reciprocal space

projected in the surface plane were the $Ni_3Al(111)$ alloy unit cell is taken as the hexagonal basis (filled circles). The lattice constants corresponding to a given radius in the reciprocal space are depicted.

As Pd clusters are more easy to prepare and measure by SXRD, due to the higher scattering power of Pd compared to Co, the oxide preparation and the possibility to measure the structural properties of the clusters was primarily tested with well-ordered Pd clusters (confirmed by GISAXS) below coalescence grown at RT. The Pd coverage was 0.25 nm. The Pd clusters grow with (111) facets on top; this is confirmed by our XRD data showing a rod at $(11)_{hex}$ with peaks at L=0 and L=2.74. A radial scan across the Pd $(1\ 1)_{hex}$ rod at L=0.06, i.e. close to the $(-2\ 0\ 2)_{cub}$ Bragg reflection expressed in cubic indices, is shown in Fig. 10(b). From the position of the fitted Gaussian distribution the spacing between $(1\ 1\ 0)_{hex}$ planes can be calculated. The double of this spacing is the in plane next neighbor distance of Pd atoms. We find $d_{Pd\text{-}Pd}$ = 0.273 nm, which is 0.8% less than the bulk next neighbor distance (0.275 nm). The interlayer spacing we found in our data is 0.2248 nm, the same as bulk Pd (0.2246) within the error bar. The Pd rod is rotated by -24.6° compared to the Ni_3Al $[\bar{1}01]$ direction (i.e. (11) in the surface cell reference) and a twin which belongs to the second rotational domain of the oxide can be found rotated by -35.4° (= 24.6° - 60°) compared to the Ni_3Al $[\bar{1}01]$ direction. Fig. 11 shows a processed STM image of 0.23 nm Pd clusters deposited at RT. The facets on top of the clusters are triangular like shaped. From the Fourier transform of a large-scale image the Ni_3Al $[1\ \bar{1}0]$ could be determined and is plotted in the figure. The angle between the Ni_3Al $[1\ \bar{1}0]$ direction and the orientation of a typical cluster measured by STM is 25° (the angle has been derived from an average of the clusters shape), a value that agrees to the data obtained from SXRD. We can now identify the angle between the oxide and the Pd

clusters to be 12.4°. However, not all clusters are perfectly parallel aligned due to a rotational degree of freedom. This manifests also in the SXRD measurements as a broad angular distribution of the Pd $(1\ 1\ 0)_{hex}$ Bragg peak.

Assuming that the Co clusters do not change their structural properties upon coalescence, as has been suggested by the STM experiments, SXRD was performed at Co coverage of 2 nm, above coalescence, to ensure a sufficiently large diffracted intensity and a large number of layers for an unambiguous determination of the rotation of Co clusters and subsequently the type of layer stacking. The clusters were grown at 470 K.

As the nearest neighbor distance of bulk Co atoms in a close-packed plane ($d_{Co\text{-}Co}$ = 0.25074 nm) is almost equal to the nearest neighbor distance of atoms in the $Ni_3Al(111)$ alloy surface, the Co $(1\ 0)_{hex}$ rod is located at the same radial distance as the $(2\ 0)_{hex}$ rod of the $Ni_3Al(111)$ alloy surface, i.e., the $(1\ 0)_{hex}$ rod of the fcc lattice of the $Ni_3Al(111)$ surface [Fig. 10(a)].

As the nearest neighbor distance of bulk Co atoms in a close-packed plane ($d_{Co\text{-}Co}$ = 0.25074 nm) is almost equal to the nearest neighbor distance of atoms in the $Ni_3Al(111)$ alloy surface, the Co $(1\ 0)_{hex}$ rod is located at the same radial distance as the (2 0) rod of the $Ni_3Al(111)$ alloy surface, i.e., the $(1\ 0)_{hex}$ rod of the fcc lattice of the $Ni_3Al(111)$ surface.

Fig. 10(c) shows a radial scan of $q_{||}$, the scattering vector component parallel to the surface, across the (2 0) rod at L=1.5. This would correspond to the (1 0 1) Bragg peak of hcp Co. An azimuthal scan at the same (H K L) shows a coincidence of the Co $(1\ 0)_{hex}$ rod with (2 0) rod of the alloy, which can be attributed to the same orientation of Co clusters as the $Ni_3Al(111)$ surface below the oxide. Due to the finite size of the clusters and to their mosaicity, the angular width of the Co rod is larger

than the that one of the $Ni_3Al(111)$ rod. Therefore the radial scan across the Co rod was taken slightly off from the peak maximum (rotated by 0.5° from the (2 0 1.5) reflection) as shown in Fig. 10(a) (grey line), minimizing the contribution from the substrate. The in plane Co lattice constant derived from the fit shown in Fig. 10(c) is 0.2503 nm (0.2% less than in bulk Co).

At first glance, the azimuthal orientation is somewhat unexpected as the corner hole has a diameter of only 0.4 nm, too small for any structure that could transfer the rotational alignment from the substrate to the cluster, and also the ring of Al and O atoms directly surrounding the corner hole is not rotationally aligned with a low-index direction of the substrate. We note, however, that the oxide around the corner holes has rows of O and Al atoms deviating by about 2° or less from the $\langle 1\ 1\ \overline{2} \rangle$ directions of the substrate. The distance between these rows is typically around 0.25 nm, thus it fits the Co-Co interatomic spacing, but not the distance between Co rows in a close-packed Co layer (0.217 nm). An overlayer with Co-Co distances parallel to the rows in the oxide will have an azimuthal orientation roughly parallel to the Ni_3Al substrate. Of course, this is not a coincidence: The orientation and distance of the O and Al rows in the oxide surface is due to the registry of the lower layers in the oxide on the Ni_3Al substrate.

I. Layer stacking of Co clusters after coalescence

Knowing the azimuthal orientation of the Co clusters we can now proceed to study the layer stacking of the Co clusters. Fig. 12(a) shows a scan along the (2 0) rod. The large peak at $q_\perp$ = 10.2 nm^{-1} can be identified as the (2 0 1) Bragg peak of the $Ni_3Al(111)$ alloy in the hexagonal cell. The scan was again performed 0.5° off the rod maximum in azimuth to increase the ratio of the desired Co signal to the (in this

measurement) interfering substrate rod. The dashed grey line shows a pseudo-Voigt fit of the Bragg peak. After subtracting this fitted bulk peak, a peak at $q_\perp = 15.1$ nm^{-1} remains [Fig. 12(b)]. This peak can be fitted by

$$I(q) = \frac{C}{5/4 + \cos(q\,d)} \quad ,$$

a function that describes the scattering power of close-packed planes with random stacking and an interlayer distance d [66] [dashed in Fig. 10(b)]. The peak in Fig. 12(b) results in d = 0.2067 ± 0.0005 nm, the interlayer distance of close-packed Co planes (0.2035 nm for Co hcp). This confirms the interlayer distance observed in the STM height histograms.

Hence, we conclude that Co clusters grow with roughly the same azimuthal orientation as the $Ni_3Al(111)$ surface below the oxide and with random stacking of close-packed planes on top of the corner holes.

IV. Summary

We have demonstrated the applicability of alumina on $Ni_3Al(111)$ as a template with a 4.1 nm lattice for growing highly ordered clusters of Co as well as Fe. Pd atoms trapped in the corner holes of the oxide create metallic nucleation sites where Fe or Co can nucleate and form a well-ordered hexagonal arrangement on the oxide nanomesh. We have studied the morphology of these Fe and Co clusters and applied different methods like STM, XRD and GISAXS to determine the morphology and crystallographic properties of the clusters.

Fe clusters grow exclusively on top of the Pd atoms in the corner holes at temperatures ranging from RT up to 570 K. Co clusters deposited at RT nucleate at the Pd-filled corner holes, but also on a second site with 3-fold symmetry. Nucleation on these 3-fold sites can be avoided by deposition above 470 K, where also Co

nucleates exclusively on top of the Pd atoms in the corner holes. As shown for Fe clusters without predeposition of Pd, our study also demonstrates that sharp spots in the Fourier transform of the cluster positions do not imply good ordering of the clusters. We explain the differences of cluster growth with and without Pd atoms in the corner holes by an energy barrier for diffusion of Fe and Co atoms into the corner holes. This energy barrier is small or vanishes for Pd atoms, allowing them to jump into the corner hole, which is the energetically most favorable nucleation site. The distance between the clusters of 4.1 nm, rather large for self-organized templates, and the high contact angles make it possible to grow fairly large clusters (≈1000 atoms) before coalescence occurs and the high degree of ordering disappears.

Fe clusters deposited at RT grow with bcc (100) planes parallel to the substrate surface; clusters grown at elevated temperatures (above 470 K) have bcc (110) orientation. Co clusters exhibit close-packed planes on top in the temperature range for growing well-ordered clusters (470 –570 K). XRD measurements have shown that these Co clusters are neither fcc nor hcp but possess random stacking of close-packed planes.

V. Acknowledgement

This work was financially supported by the Austrian Fonds zur Förderung der wissenschaftlichen Forschung. Beam time at ESRF is acknowledged.

References

[1]P. Ohresser, N. B. Brookes, S. Padovani, F. Scheurer, and H. Bulou. *Phys. Rev. B* **64**, 104429 (2001).
[2]B D Terris and T Thomson, J. Phys. D: Appl. Phys. 38 R199-R222 (2005)
[3]N. Weiss, T. Cren, M. Epple, S. Rusponi, G. Baudot, S. Rohart, A. Tejeda, V. Repain, S. Rousset, P. Ohresser, F. Scheurer, P. Bencok, and H. Brune, *Phys. Rev. Lett.* **95**, 157204 (2005).

[4]S. Rohart, V. Repain, A. Tejeda, P. Ohresser, F. Scheurer, P. Bencok, J. Ferre, and S. Rousset, Phys. Rev. B **73**, 165412 (2006).
[5]J. Y. Yang, K. S. Yoon, Y. H. Do, J. H. Kim, J. H. Lee, C. O. Kim, J. P. Hong, E. K. Kim, *IEEE Trans. Magn.,* **41**, 3313-3315 (2005).
[6]C. Petit, S. Rusponi, H. Brune, *J. Appl. Phys.* **95**, 4251-4260 (2004).
[7]Brune, H., *Physics and Engineering of New Materials* (Springer, Berlin, 2009) Vol. 127, p. 123.
[8]H. Brune, P. Gambardella, *Surf. Sci.,* **603**, 1812-1830 (2009).
[9]G. Moulas, A. Lehnert, S. Rusponi, J. Zabloudil, C. Etz, S. Ouazi, M. Etzkorn, P. Bencok, P. Gambardella, P. Weinberger, and H. Brune, *Phys. Rev. B* **78**, 214424 (2008).
[10]P. Gambardella, S. Rusponi, M. Veronese, S. S. Dhesi, C. Grazioli, A. Dallmeyer, I. Cabria, R. Zeller, P. H. Dederichs, K. Kern, C. Carbone, H. Brune, *Science* **300**, 1130-1133 (2003).
[11]T. Cren, S. Rusponi, N. Weiss, M. Epple, H. Brune, *J. Phys. Chem. B,* **108**, 14685-14691(2004).
[12]H. Brune, S. Rusponi, The Chemical Physics of Solid Surfaces **12**, 427-470 (2007).
[13]S. I. Woods, J. R. Kirtley, Shouheng Sun, R. H. Koch, *Phys. Rev. Lett.* **87**, 137205 (2001).
[14]C. Petit, A. Taleb, M. P. Pileni, *Adv. Mater.* **10**, 259-261 (1998).
[15]V. F. Puntes, K. M. Krishnan, P. Alivisatos. *Appl. Phys. Lett.* **78**, 2187-2189 (2001).
[16]C. Antoniak, J. Lindner, M. Spasova, D. Sudfeld, M. Acet, M. Farle, K. Fauth, U. Wiedwald, H. G. Boyen, P. Ziemann, F. Wilhelm, A. Rogalev, S. Sun, *Phys. Rev. Lett.* **97**, 117201 (2006).
[17]S. Sun, C. B. Murray, D. Weller, L. Folks, A. Moser , *Science* **287**, 1989-1992 (2000).
[18]W. Wernsdorfer, E. B. Orozco, K. Hasselbach, A. Benoit, B. Barbara, N. Demoncy, A. Loiseau, H. Pascard, D. Mailly, *Phys. Rev. Lett.* **78**, 1791 (1997).
[19]A.T. Bell, *Science* **299**, 1688-1691 (2003).
[20]C.R. Henry, *Surf. Sci. Rep.* **31**, 231-325 (1998).
[21]C.T. Campbell, *Surf. Sci. Rep.,* **27**, 1-111 (1997).
[22]M. Haruta, N. Yamada, T. Kobayashi, S. Iijima, *J. Catal.,* **115**, 301-309 (1989).
[23]M. Haruta, T. Kobayashi, H. Sano, N. Yamada, *Chem. Lett.* **16**, 405-408 (1987).
[24]M. Moreno-Manas, R. Pleixats, *Acc. Chem. Res.* **36**, 638-643 (2003).
[25]H. P. Kormann, G. Schmid, K. Pelzer, K. Philippot, B. Chaudret, *Z. Anorg. Allg. Chem.* **630**, 1913-1918 (2004).
[26]M. Yashima, L. K. L. Falk, A. E. C. Palmqvist, K. Holmberg, *J. Colloid Int. Sci.* **268**, 348-356 (2003).
[27]M. Heemeier, A. F. Carlsson, M. Naschitzki, M. Schmal, M. Baumer, H.-J. Freund, Angew. Chem. Int. Ed. **41**, 4073-4076 (2002).
[28]S. Schauermann, J. Hoffmann, V. Johánek, J. Hartmann, J. Libuda, H.-J. Freund, *Angew. Chem. Int. Ed.* **41**, 2532-2535 (2002).

[29]S. Sun, C.B. Murray, *J. Appl. Phys.* **85**, 4325-4330 (1999).
[30]K. At-Mansour, A. Buchsbaum, P. Ruffieux, M. Schmid, P. Grning, P. Varga, R. Fasel, O. Gröning, *Nano Lett.* **8**, 2035-2040 (2008).
[31]S. Berner, M. Corso, R. Widmer, O. Groening, R. Laskowski, P. Blaha, K. Schwarz, A. Goriachko, H. Over, S. Gsell, M. Schreck, H. Sachdev, T. Greber, J. Osterwalder, *Angew. Chem. Int. Ed.* **46**, 5115-5119 (2007).

[32]M. Corso, W. Auwärter, M. Muntwiler, A. Tamai, T. Greber, J. Osterwalder, *Science* **303**, 217-220 (2004).
[33]H. Brune, M. Giovannini, K. Bromann , K. Kern , *Nature* **394**, 451-453 (1998).
[34]T. Classen, G. Fratesi, G. Costantini, S. Fabris, F. L. Stadler, C. Kim, S. de Gironcoli, S. Baroni, K. Kern, *Angew. Chem. Int. Ed.* **44**, 6142-6145 (2005).
[35]S. W. Kim, S. U. Son, S. S. Lee, T. Hyeon, Y. K. Chung . *Chem. Commun.* 2212-2213 (2001).
[36]K.H. Park, S.U. Son, Y.K. Chung, ,*Organ. Lett.* **4**, 4361-4363 (2002).
[37]R. Burch, *Catal. Rev.* **46**, 271 (2004).
[38]K. Shimizu, A. Satsuma, *Phys. Chem. Chem. Phys.* **8**, 2677-2695 (2006).
[39]H. Over, O. Balmes, E. Lundgren, *Surf. Sci.* **603**, 298-303 (2009).
[40]B. L. M. Hendriksen, J. W. M. Frenken, *Phys. Rev. Lett.* **89**, 046101 (2002).
[41]R. Westerström, J. G. Wang, M. Ackermann, J. Gustafson, A. Resta, A. Mikkelsen, J. N. Andersen, E. Lundgren, O. Balmes, X. Torrelles, J. W. M. Frenken, B. Hammer, *J. Phys.: Condens. Matter* **20**, 184018 (2008).
[42]G. Rupprechter, C. Weilach, *J. Phys.: Condens. Matter* **20**, 184019 (2008).
[43]M. Schmid, G. Kresse, A. Buchsbaum, E. Napetschnig, S. Gritschneder, M. Reichling, P. Varga, *Phys. Rev. Lett.* **99**, 196104-4 (2007).
[44]S. Degen, C. Becker, K. Wandelt, *Faraday Disc.* **125**, 343-356 (2004).
[45]G. Hamm, C. Becker, C. R. Henry, *Nanotechnology* **17**, 1943-1947 (2006).
[46]C. Becker, A. Rosenhahn, A. Wiltner, K. von Bergmann, J. Schneider, P. Pervan, M. Milun, M. Kralj, K. Wandelt, *New J. Phys.* **4**, 75 (2002).
[47]C. Becker, K. von Bergmann, A. Rosenhahn, J. Schneider, K. Wandelt, *Surf. Sci.* **486**, L443-L448 (2001).
[48]A. Lehnert, A. Krupski, S. Degen, K. Franke, R. Decker, S. Rusponi, M. Kralj, C. Becker, H. Brune, K. Wandelt, *Surf. Sci.* **600**, 1804-1808 (2006).
[49]S. Gritschneder, S. Degen, C. Becker, K. Wandelt, M. Reichling, *Phys. Rev. B* **76**, 014123-5 (2007).
[50]C. Nagl, O. Haller, E. Platzgummer, M. Schmid, P. Varga, *Surf. Sci.* **321**, 237-248 (1994).
[51]B. L. Henke, E. M. Gullikson, J. C. Davis, *At. Data Nucl. Data Tables* **54**, 181-342 (1993).
[52]S. Degen, A. Krupski, M. Kralj, A. Langner, C. Becker, M. Sokolowski, K. Wandelt, *Surf. Sci.* **576**, L57-L64 (2005).
[53]A. Rosenhahn, J. Schneider, C. Becker, K. Wandelt, J. Vac. Sci. Technol. A 18, 1923 (2000).
[54]N. Eustathopoulos, B. Drevet, *J. Phys. III France* **4** 1865-1881 (1994)
[55]H. Brune, *Landolt Börnstein Series: Physics of Covered Solid Surfaces*, (Springer, Berlin, 2001), Vol. 42A, p. 217.
[56]E. Napetschnig, M. Schmid, P. Varga, *Surf. Sci.* **601**, 3233-3245 (2007).
[57]G. Ehrlich, F. G. Hudda, *J. Chem. Phys.* **44**, 1039-1049 (1966).
[58]R. L. Schwoebel, E. J. Shipsey, *J. Appl. Phys.* **37**, 3682-3686 (1966).
[59]W. Hebenstreit, J. Redinger,Z. Horozova, M. Schmid, R. Podloucky, P. Varga, *Surf. Sci.* **424**, L321-L328 (1999).
[60]K. Hojrup Hansen, T. Worren, E. Laegsgaard, F. Besenbacher, I. Stensgaard, *Surf. Sci.* **475**, 96-102 (2001).
[61]D. C. Lim, I. Lopez-Salido, R. Dietsche, M. Bubek, Y. D. Kim, *Chem. Phys.* **330**, 441-448 (2006).
[62]D. Weller, G. R. Harp, R. F. C. Farrow, A. Cebollada, J. Sticht, *Phys. Rev. Lett.* **72**, 2097 (1994).

[63]D. Weller, A. Carl, R. Savoy, T.C. Huang, M.F. Toney, C. Chappert. *J. Phys. Chem. Sol.* **56**, 1563-1566 (1995).
[64]G. R. Harp, R. F. C. Farrow, D. Weller, T. A. Rabedeau, R. F. Marks, *Phys. Rev. B* **48**, 17538 (1993).
[65]S. Park, X. Zhang, A. Misra, J. D. Thompson, M. R. Fitzsimmons, S. Lee, C. M. Falco, *Appl. Phys. Lett.* **86**, 042504-3 (2005).
[66]A. Guinier, *X-Ray Diffraction in Crystals, Imperfect Crystals, and Amorphous Bodies* (Dover Publications, Inc., New York, 1994), p. 230.

	Fe					Co		
Deposition at T (K)	RT	370	470	470	570	470 K	470	570
Coverage Θ (nm)	0.06	0.06	0.06	0.1	0.1	0.06	0.1	0.1
Atoms/cluster	107	98	112	161	160	80	145	145
average height h_{avg} (nm)	0.6	0.7	0.81	0.89	0.84	0.62	0.81	0.85
contact angle φ	57	73	83	80	79	71	75	82
Diameter d (nm)	2.2	1.84	1.8	2.1	2.2	1.8	1.7	1.8

Tab. 1 Properties of the Fe and Co clusters determined from the height distributions.

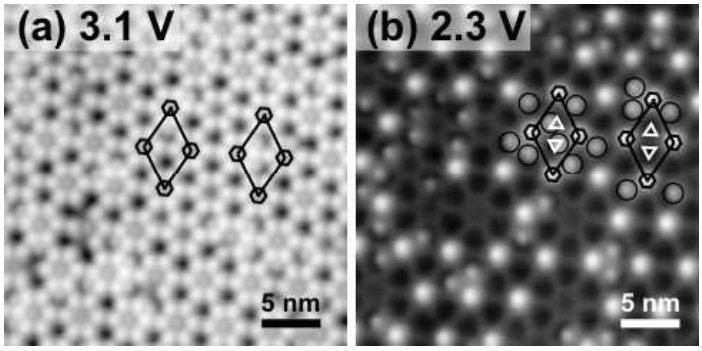

Fig .1. STM images taken at 3.1 V/0.1 nA (a) where the net structure appears and at 2.3 V/0.1 nA (b) showing the dot structure. The unit cell is drawn in black with the corner holes as hexagons, triangles mark the 3-fold sites and circles mark the defects. The sketch on the right side shows possible nucleation sites for Co and Fe clusters at RT.

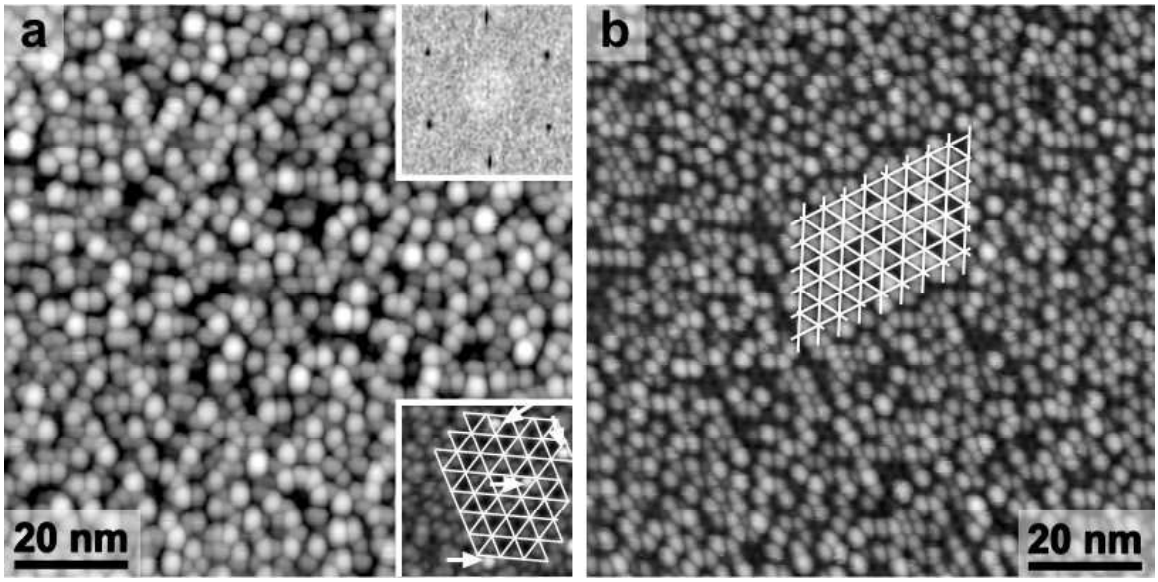

Fig. 2. STM images (3.1 V/0.1 nA) of (a) 0.1 nm Fe and (b) 0.06 nm Co deposited at RT. The cross points of the white grids mark the corner holes. The upper inset of (a) shows a Fourier transform of the clusters centers in the STM image and the lower one an STM image (2.3 V/ 0.1 nA) of 0.01 nm Fe where Fe clusters are marked with white arrows.

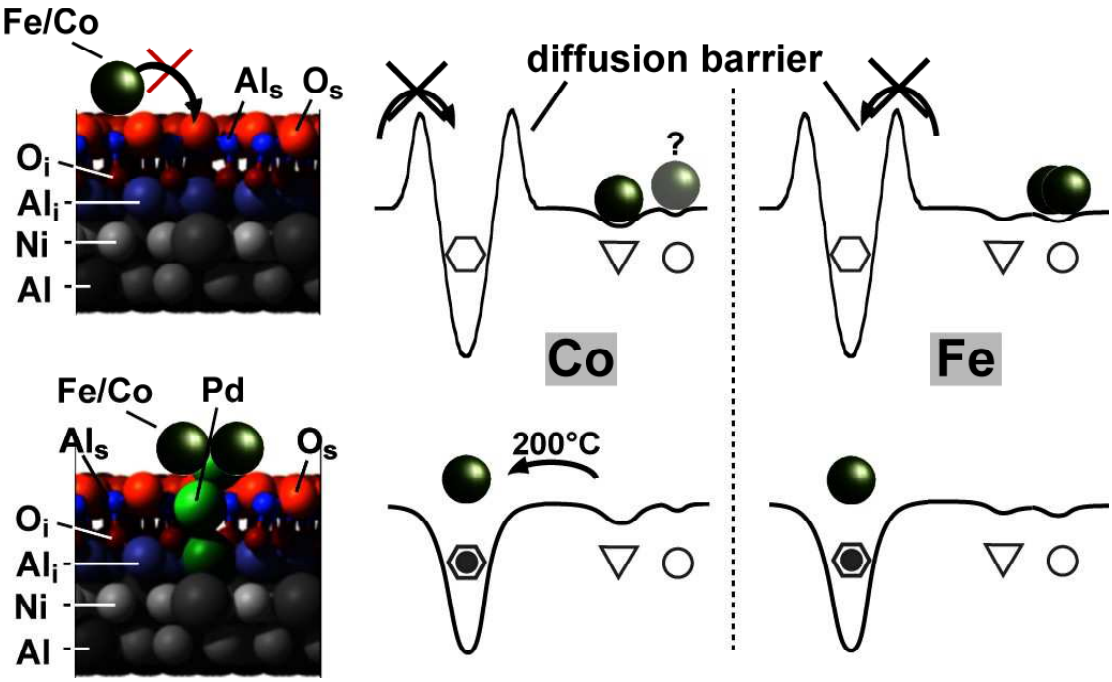

Fig. 3. (a) Side view of the corner hole of the oxide with a nearby Fe or Co atom on top. (b) Schematic drawing of the potential energy surface for Fe as well as Co atoms. Empty hexagons symbolize the corner holes, filled hexagons the corner holes filled by 3 Pd atoms each, triangles are the 3-fold sites of the unit cell and circles are the defects (see also Fig. 1).

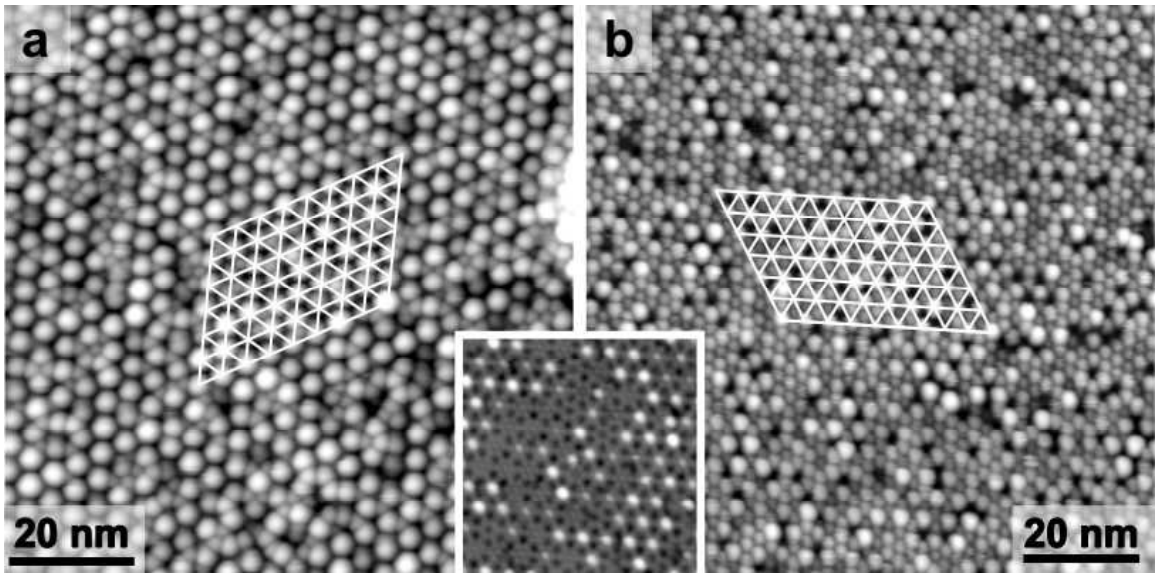

Fig. 4. STM images (3.1 V/ 0.1 nA) of 0.1 nm Fe (a) and 0.06 nm Co (b) deposited at RT (Pd seeded). The cross points of the white grids mark the corner holes. The inset in the center shows an STM image (3.1 V/ 0.1 nA) of the oxide with corner holes filled by 3 Pd atoms (bright dots) as it was taken previous to all cluster deposition experiments.

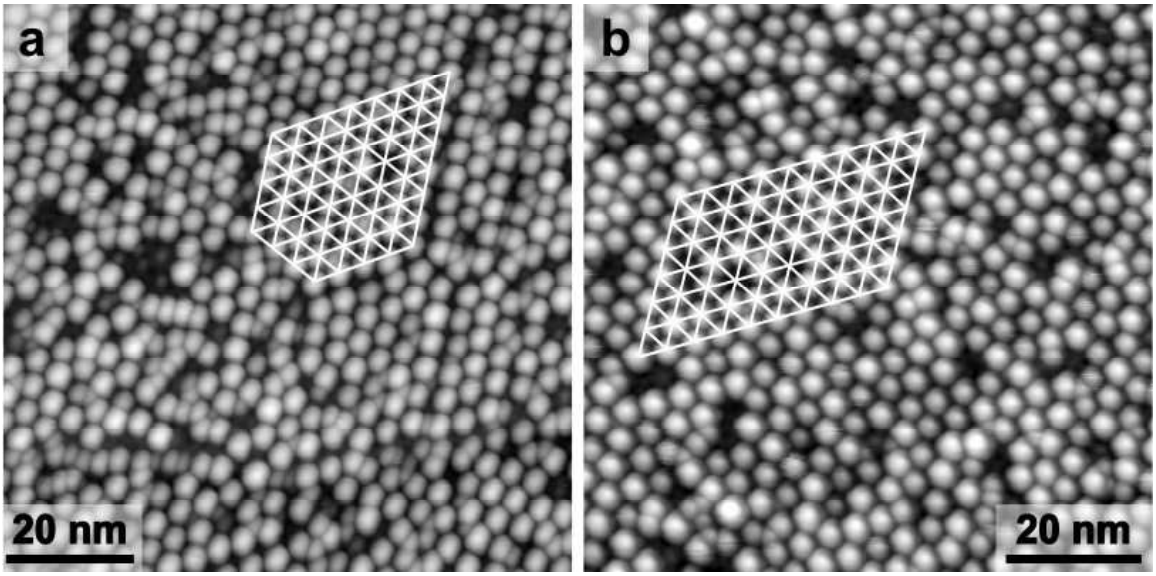

Fig. 5. STM images (3.1 V/ 0.1 nA) of 0.1 nm Fe (a) and 0.06 nm Co (b) deposited at 470 K (Pd seeded). The cross points of the white grids mark the corner holes.

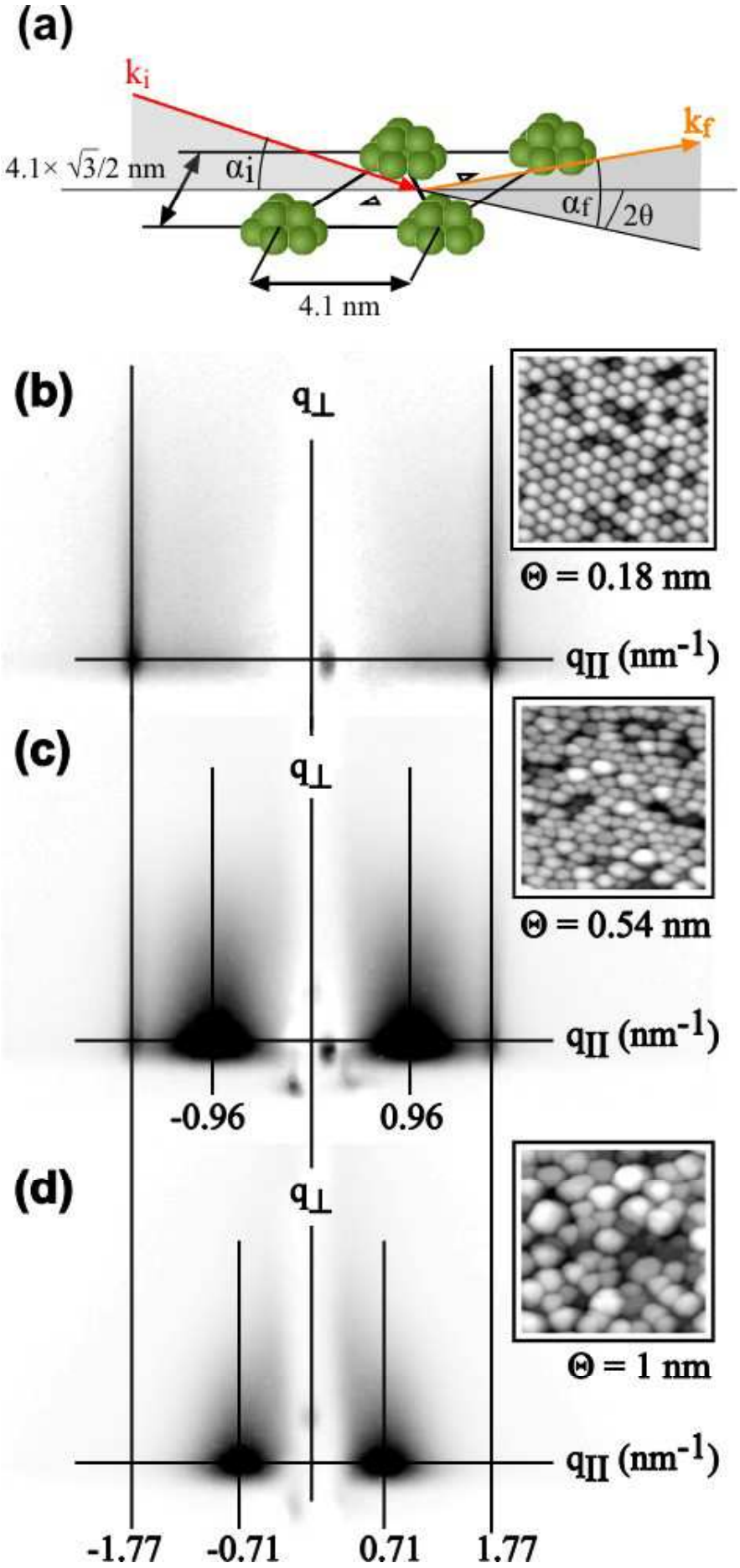
(a)
k_i
k_f
4.1× √3/2 nm
α_i
α_f
2θ
4.1 nm
(b)
$q_\perp$
Θ = 0.18 nm
q_{II} (nm^{-1})
(c)
$q_\perp$
Θ = 0.54 nm
q_{II} (nm^{-1})
-0.96
0.96
(d)
$q_\perp$
Θ = 1 nm
q_{II} (nm^{-1})
-1.77
-0.71
0.71
1.77

Fig. 6. (a) Sketch of the beam alignment with respect to the cluster arrangement in real space. In-situ GISAXS measurements taken at coverages of (b) Θ = 0.18 nm Co (c) Θ = 0.54 nm Co and (d) Θ = 1 nm Co, respectively deposited at 470 K (Pd seeded). The insets are STM images (3.1 V/ 0.1 nA) taken at equal experimental conditions each of them 50 nm wide.

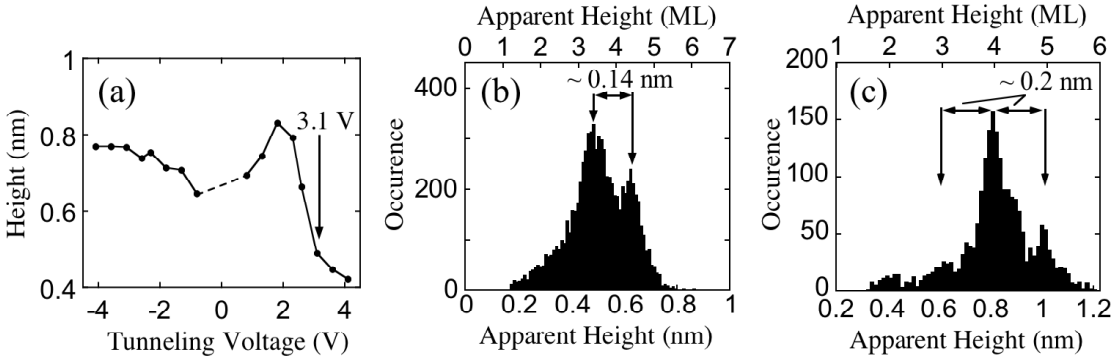

Fig. 7. (a) Apparent average height vs. tunneling voltage of 0.06 nm Fe clusters deposited at RT (Pd seeded), (b) height histogram of the same preparation taken at 3.1 V and (c) height histogram of 0.1 nm Fe deposited at 570 K (Pd seeded). The STM images were taken at 0.1 nA keeping the position of the STM tip constant.

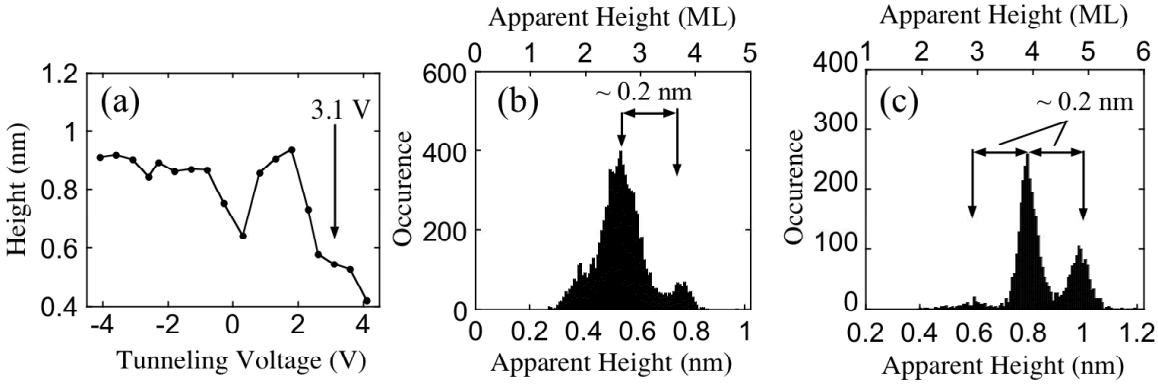

Fig. 8. (a) Apparent average height vs. tunneling voltage of 0.06 nm Co clusters deposited at 470 K (Pd seeded), (b) height histogram of the same preparation taken at

3.1 V and (c) height histogram of 0.1 nm Co deposited at 570 K (Pd seeded). The STM images were taken at 0.1 nA keeping the position of the STM tip constant.

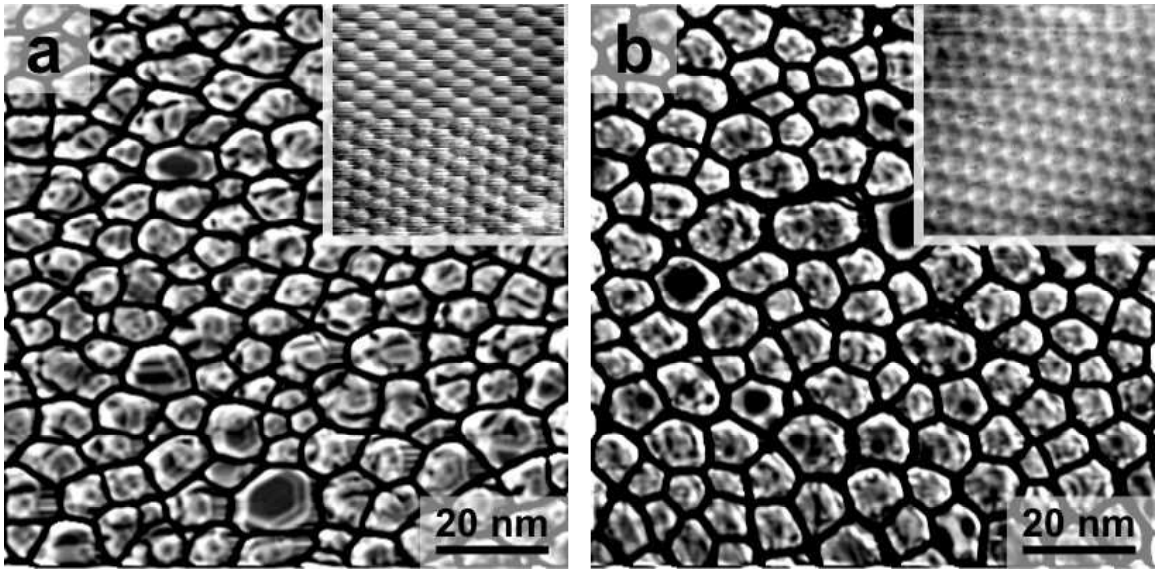

Fig. 9. STM images (3.1 V/ 0.1 nA) of 2.8 nm Fe (a) and 2.8 nm Co (b) deposited at 470 K (Pd seeded). The images are high-pass filtered to reveal the morphology of the clusters. The insets show STM images with atomic resolution taken on flat facets on top of flat clusters visible in the large STM images.

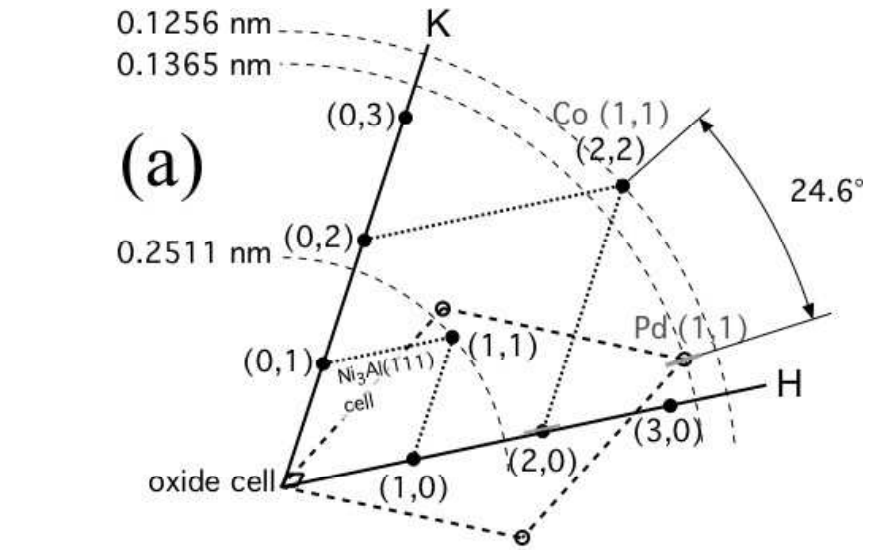
0.1256 nm
0.1365 nm
K
(0,3)
Co (1,1)
(2,2)
(a)
24.6°
0.2511 nm
(0,2)
Pd (1,1)
(1,1)
(0,1)
Ni3Al(111)
cell
H
(3,0)
(2,0)
oxide cell
(1,0)

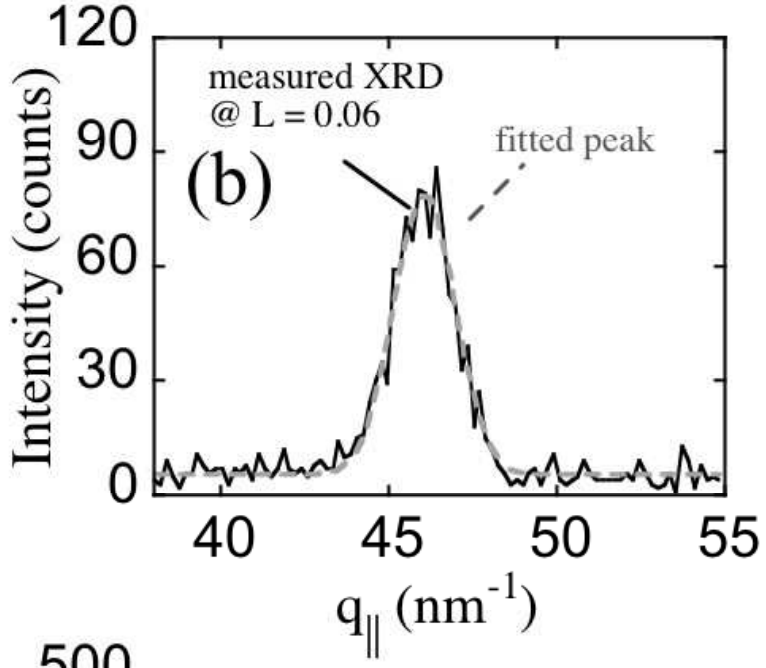
measured XRD
@ L = 0.06
fitted peak
(b)
Intensity (counts)
120
90
60
30
0
40
45
50
55
q|| (nm-1)

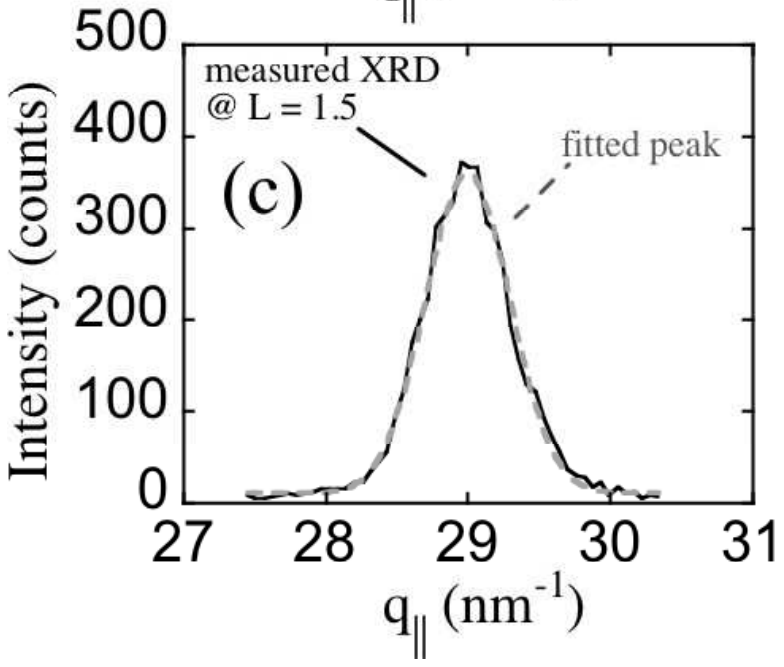
measured XRD
@ L = 1.5
fitted peak
(c)
Intensity (counts)
500
400
300
200
100
0
27
28
29
30
31
q|| (nm-1)

Fig. 10. (a) Map of the reciprocal space of the $Ni_3Al(111)$ alloy cell (H = 1, K =1), the oxide cell and the Pd as well as the Co unit cell. The radial gray lines at the Pd (1, 1) and the Co (1, 0) reciprocal lattice points mark the positions of the scans shown below. (b) Radial XRD scan across the Pd (1, 1, 0) Bragg peak and (c) radial scan across the Co (1, 0, 1.5) Bragg peak.

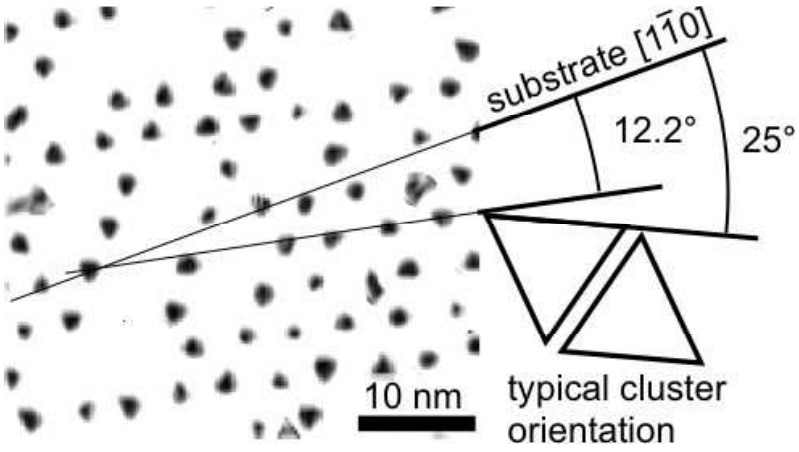

Fig. 11. Processed STM image of 0.23 nm Pd clusters deposited at RT. The substrate [1 $\bar{1}$0] has been identified on a large scale STM image from the same experiment were both oxide orientation were present. The typical orientation of the Pd clusters is 25° related to the close-packed Ni_3Al rows.

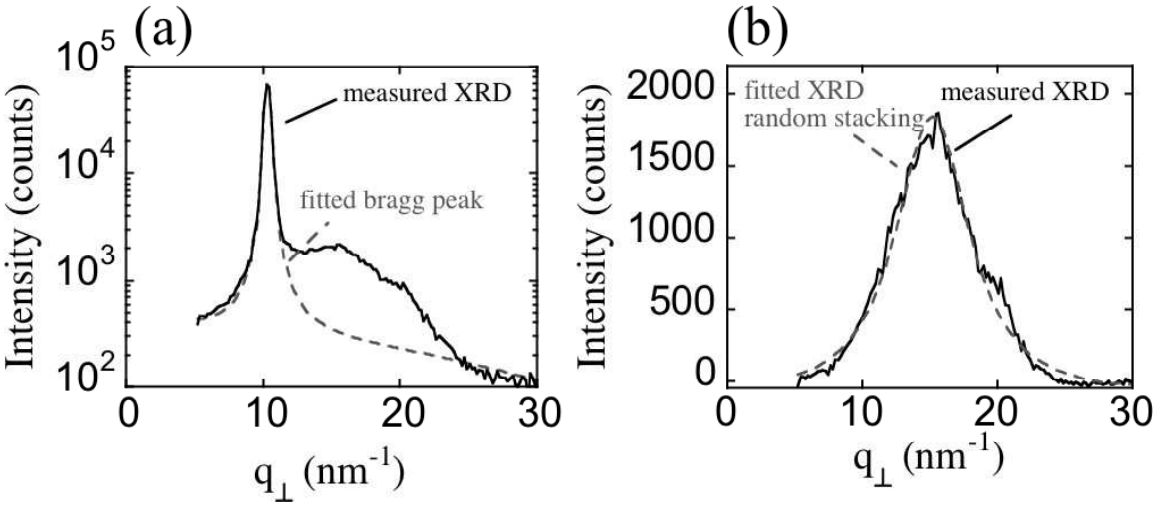

Fig. 12. (2 0) rod of the surface after deposition of 2 nm Co clusters deposited at 470 K (Pd seeded), indexed in the alloy hexagonal cell. (a) with the Bragg peak of $Ni_3Al(111)$ at $q_\perp = 10.2$ nm^{-1} (L = 1) fitted by a pseudo-Voigt function and (b) after Bragg peak subtraction. This corresponds to the $(1\ 0)_{hex}$ rod of a Co hcp (001) or fcc(111) surface. The peak is fitted by a function assigned to random stacking of close-packed planes.